Chemical Synthesis

Research Article

In situ synthesis of nanosized ZSM-12 zeolite isomorphously substituted by gallium for the *n*-hexadecane hydroisomerization

Hailong Lin, Chang Xu, Wei Wang[*] iD **, Wei Wu**[*] iD

National Center for International Research on Catalytic Technology, Key Laboratory of Functional Inorganic Materials Chemistry (Ministry of Education), School of Chemistry and Material Sciences, Heilongjiang University, Harbin 150080, Heilongjiang, China.

[*]**Correspondence to:** Prof. Wei Wang, Prof. Wei Wu, National Center for International Research on Catalytic Technology, Key Laboratory of Functional Inorganic Materials Chemistry (Ministry of Education), School of Chemistry and Material Sciences, Heilongjiang University, No. 74 Xuefu Road, Nangang District, Harbin 150080, Heilongjiang, China. E-mail: wangw@hlju.edu.cn; wuwei@hlju.edu.cn

Abstract

The ZSM-12 zeolite has attracted attention as the promising acid component of bifunctional catalysts for the *n*-alkane hydroisomerization because of its large size of micropore openings (0.57 nm × 0.61 nm) with 12-membered-ring and one-dimensional channels. However, the larger crystal size and stronger Brønsted acid strength of microsized ZSM-12 zeolite will lead to cracking of *iso*-olefin intermediates and decrease the *iso*-alkane yield. In this study, ZSM-12 zeolite samples partially and completely isomorphously substituted with gallium ([Ga,Al]Z12 and GaZ12) were *in situ* synthesized. The characteristic results indicate that isomorphous substitution by Ga can effectively reduce the crystal size to increase the mesoporosity and weaken the Brønsted acidity of the [Ga,Al]Z12 and GaZ12 samples. In addition, bifunctional catalysts with more appropriate metal-acid proximity for *n*-hexadecane hydroisomerization were prepared by mixing the 0.6Pd/A sample with 0.6 wt.% Pd loaded on γ-Al$_2$O$_3$ and the ZSM-12, [Ga,Al]Z12 and GaZ12 samples, respectively. The 0.3Pd/A-[Ga,Al]Z12 and 0.3Pd/A-GaZ12 catalysts both promote the maximum *iso*-hexadecane yield and distribution of multi-branched *iso*-hexadecane products due to their enhanced mesoporosity, reduced Brønsted acid strength, increased C_{Pd}/C_{H+} ratios and improved metal-acid balance. Especially for the 0.3Pd/A-GaZ12 catalyst, when the *n*-hexadecane conversion is 93.5%, the maximum *iso*-hexadecane yield reaches 80.6%, and the proportion of multi-branched *iso*-hexadecane products is 64.6%, which are both the highest among all investigated catalysts. Accordingly, Ga

isomorphous substitution is an effective strategy to develop the efficient bifunctional catalysts for hydroisomerization.

INTRODUCTION

Owing to the reduction in non-renewable fossil energy and increasing environmental awareness, the development of high-quality alternative energy sources has attracted worldwide attention in recent decades[1-5]. Second-generation biodiesel has become a potential environmentally friendly fuel because of its abundant and renewable raw materials, which are free of olefins, aromatics, sulfides, and nitrides[6,7]. To modify the low-temperature flow property of second-generation biodiesel produced from Fischer-Tropsch synthesis wax or vegetable oil, the hydroisomerization of linear *n*-alkanes with long carbon chains has become an essential process[8-10]. Currently, the most widely employed catalysts for *n*-alkane hydroisomerization are bifunctional catalysts containing metal sites with dehydrogenation and hydrogenation functions and Brønsted acid sites with isomerization functions[11,12]. Accordingly, it is essential to develop effective bifunctional catalysts to improve the hydroisomerization performance of *n*-alkanes and, thus, the quality of produced biodiesel.

ZSM-12 zeolite with a 12-membered-ring opening has become a promising acid support for providing Brønsted acid sites because of its one-dimensional channels and large opening size of main channels (0.57 nm × 0.61 nm), which is beneficial to improve the mass transfer properties[13,14]. However, since the diffusion of intermediates and products is evidently limited in the micropores of ZSM-12 zeolite, the interaction between the intermediates and the Brønsted acid sites is enhanced, which leads to reduced yield of ideal isomerized alkane products due to the enhanced cracking. Accordingly, synthesizing hierarchical ZSM-12 zeolite to shorten the diffusion distance in the channel and reduce Brønsted acid strength has been proven to be an effective method for suppressing the cracking of hydrocarbons[15,16]. The hierarchical zeolites are generally synthesized by two methods. One is the top-down strategy to form intracrystalline mesopores by removing framework Si atoms or framework Al atoms via the post-treatment method[17,18]. The other way is to generate intercrystal mesopores by reducing the crystal size via a bottom-up strategy using mesoporous templates or crystal growth inhibitors[19,20]. However, during post-treatment, a large amount of wastewater is generated, and the synthesized hierarchical zeolites usually reveal weaker stability due to the removal of framework atoms[21]. While for synthesis by using additional expensive mesoporous templates, the crystallization conditions are usually strict, and the synthesis process is commonly complicated[22]. Therefore, developing a simple and inexpensive method for the *in situ* synthesis of nanosized ZSM-12 zeolites with higher mesoporosity and lower Brønsted acid strength is still essential to avoid the above disadvantages.

In recent years, the synthesis of metal-incorporated zeolites containing Zn, Fe and Ga in the framework has been recognized as a promising method to decrease the crystal size and weaken the acidity of synthesized hierarchical zeolites simultaneously[23,24]. Because of the larger atomic radius, the substitution of Ga and Fe into the framework is more difficult, and the H^+ dissociation of Ga-OH-Si and Fe-OH-Si groups is also weaker than that of the Al-OH-Si group. Accordingly, Ga- or Fe-containing zeolites generally have weaker Brønsted acidity than conventional silica aluminate zeolites[25,26]. To synthesize Ga-incorporated zeolite, the conventional strategies are ion exchange and wet impregnation methods. However, the Ga amount introduced into the ion exchange sites of the ZSM-12 zeolite is generally limited because of the high Si/Al

ratios[27]. Additionally, for the preparation of Ga-incorporated zeolites by the incipient wet impregnation method, most of the Ga species are still located on the external surface or enriched at the micropores opening of the zeolite and finally become aggregated Ga oxides after the preparation of the bifunctional catalysts[28].

In addition to ion exchange and impregnation strategies, isomorphous substitution has been developed as a promising method for synthesizing Ga-incorporated zeolites due to its simple synthesis process and wide range of adjustable acidity[29,30]. Yang *et al.* synthesized Ga-substituted HZM-5 zeolites via a hydrothermal process by adding different amounts of $Ga(NO_3)_3$ to the initial gel and studied their catalytic performances for the *in situ* reforming of lignite pyrolysis volatiles to enrich light aromatics. The catalytic test results suggest that the benzene yield over Ga-substituted HZM-5 zeolite is almost two times greater than that over conventional HZSM-5 zeolite[31]. Liu *et al.* synthesized Ga-ZSM-22 zeolites as supports for the *n*-dodecane hydroisomerization. They found that the selectivity for *iso*-dodecanes increased from 47.01% to 78.19% after Ga substitution since the synthesized Ga-substituted ZSM-22 zeolites demonstrated reduced Brønsted acid strength and acid density[32]. Although the influences of Ga substitution on the catalytic performance of ZSM-5 and ZSM-22 zeolites have been investigated in the previously reported works, there have been few reports on Ga-modified ZSM-12 zeolites for the long-chain *n*-alkane hydroisomerization. Simultaneously, during the *in situ* isomorphic substitution process, the competition for the entrance into the zeolite framework between Ga and Al usually leads to the formation of abundant non-framework species that decrease the crystallinity or block micropores of synthesized zeolites, resulting in decrease of the selectivity for branched isomers. Therefore, the Ga isomorphic substitution of ZSM-12 zeolite remains challenging for the synthesis of highly effective hierarchical zeolites for hydroisomerization.

Herein, nanosized GaZSM-12 silicogalliate zeolite was synthesized *in situ* via a hydrothermal method. For comparison, [Ga,Al]ZSM-12 samples (Ga/Al molar ratio of 1:1) partially isomorphously substituted with gallium and ZSM-12 silica aluminate zeolite were also synthesized. Furthermore, bifunctional catalysts for *n*-hexadecane hydroisomerization were prepared by mixing $0.6Pd/Al_2O_3$ and synthesized Z12, [Ga,Al]Z12 and GaZ12 samples, respectively. The influences of the Ga amount of the Ga-substituted ZSM-12 samples on the textural properties, Brønsted acidity and catalytic performance of the corresponding bifunctional catalysts in *n*-hexadecane hydroisomerization were investigated.

EXPERIMENTAL

Materials
Sodium aluminate [chemically pure (CP), Sinopharm Chemical Reagent, China], silica sol (SiO_2 32.3%, Qingdao Yuminyuan, China), sodium hydroxide [analytical reagent (AR), Tianjin Tianda Chemical Reagent, China], tetraethyl ammonium bromide (TEABr, AR, Sinopharm Chemical Reagent, China) and gallium oxide (99.99%, Tianjin Guangfu Fine Chemical Research Institute, China) were used as aluminum, silica, alkaline, template and gallium sources to synthesize ZSM-12 and Ga isomorphously substituted GaZSM-12 samples, respectively. Pseudoboehmite (71%, Shandong Aluminum, China) and 5% $Pd(NO_3)_2$ aqueous solution (Shanxi Kaida, China) were used to prepare Pd/Al_2O_3 and further bifunctional catalysts.

Synthesis of Z12, [Ga,Al]Z12 and GaZ12 samples partially and completely isomorphously substituted by gallium
The ZSM-12 sample was synthesized via a hydrothermal crystallization method. The NaOH, $NaAlO_2$ and TEABr were first dissolved in deionized water, followed by the addition of silica sol under vigorous stirring to obtain the initial gel with a molar composition of $130SiO_2:1.0Al_2O_3:4.225Na_2O:16.25TEA^+:1690H_2O$. The obtained initial gel was then moved into a Teflon-lined autoclave, followed by crystallization at 160 °C for three days. After crystallization, the sample was centrifuged, washed, dried for 12 h at 110 °C, and calcined

for 6 h at 650 °C in air with a heating rate of 10 °C/min to obtain a Na-type ZSM-12 sample. Finally, the Na-type ZSM-12 sample was mixed with 0.5 mol/L NH_4NO_3 solution at a liquid/solid ratio of 30:1 for 3 h, followed by drying and calcination to obtain the H-type ZSM-12 sample, which is denoted as Z12.

The nanosized Ga partially isomorphously substituted ZSM-12 sample was synthesized by the same process except that the initial gel was prepared with a molar composition of $130SiO_2:0.5Al_2O_3:0.5Ga_2O_3:4.225Na_2O:16.25TEA^+:1690H_2O$ (with a Ga/Al molar ratio of 1), and Ga_2O_3 was first dissolved in NaOH solution. The synthesized sample is denoted as [Ga,Al]Z12.

To synthesize the nanosized Ga completely isomorphously substituted ZSM-12 sample, the same method as the [Ga,Al]Z12 sample was employed except that the initial gel was prepared with a molar composition of $130SiO_2:1Ga_2O_3:4.225Na_2O:16.25TEA^+:1690H_2O$. The synthesized sample was named GaZ12.

The preparation of bifunctional catalysts

To prepare the bifunctional catalysts, the pseudoboehmite was first calcined in air at 600 °C for 5 h with a heating rate of 10 °C/min to obtain the γ-Al_2O_3 support. Then, take 0.6 mL of the 5% $Pd(NO_3)_2$ aqueous solution and dilute it to 5.5 mL. After that, the 5 g obtained γ-Al_2O_3 was wetness-impregnated in the diluted $Pd(NO_3)_2$ aqueous solution to achieve the Pd loading of the final sample of 0.6 wt.%. The impregnated sample was then dried for 12 h at 110 °C and calcined for 4 h at 600 °C in air with a heating rate of 10 °C/min to obtain the 0.6Pd/A sample. Then, the 0.6Pd/A sample was mixed with the same mass of the Z12, [Ga,Al]Z12 and GaZ12 samples, crushed into 20-40 mesh particles and reduced in a fixed bed reactor at 400 °C for 1 h in a hydrogen atmosphere. The obtained bifunctional catalysts were named 0.3Pd/A-Z12, 0.3Pd/A-[Ga,Al]Z12 and 0.3Pd/A-GaZ12 with a final Pd loading of 0.3 wt.%.

Characterizations

All zeolite samples were analyzed using the X-ray powder diffractometer (XRD) with a Bruker D8 Advance diffractometer, which has a Cu Kα X-ray source (λ = 1.5406 Å) with the tube voltage of 40 kV and the tube current of 20 mA. The scanning angle range of 2θ = 5°-55° and the relative crystallinity of all samples were obtained by calculating the area of the characteristic diffraction peak of 2θ. The textural properties of all samples were measured by Autosorb-iQ2 automatic specific surface and porosity analyzer. The high temperature (300 °C) vacuum pretreatment was carried out in the degassing station at 1.0×10^{-3} Pa for 12 h to remove impurities. After the pretreatment, the sample tube was then transferred to a workstation, and nitrogen was adsorbed to saturation at the temperature of liquid nitrogen, and then heated at a certain rate to record the signals of N_2 adsorption and desorption. The SIGMA500 microscope was employed to investigate the morphology of all samples observed by scanning electron microscopy (SEM), and a JEM-F200 microscope was employed to investigate the morphology of synthesized ZSM-12 crystal and distribution of elements by transmission electron microscopy (TEM) at 200 kV. The ^{29}Si, ^{27}Al and ^{71}Ga magic angle spinning nuclear magnetic resonance (MAS NMR) spectra were all acquired on a Bruker advanced 400M spectrometer by loading samples into a 4 mm ZrO_2 rotor at room temperature and a magnetic field of 9.4 T and rotating at 10, 10 and 12 kHz, respectively. The framework $Si/(Al+Ga)_F$ ratio was calculated by Equation (1):

$$\frac{Si}{Al} = \frac{\sum_{n=0}^{4} I\,Si(nAl)}{\sum_{n=0}^{4} 0.25*n*I\,Si(nAl)} \tag{1}$$

in which I represents the resonance peak area in ^{29}Si MAS NMR while n indicates the number of Al atoms connected to Si. The acidity of all samples was characterized by temperature-programmed desorption (TPD) with NH_3 as a probe molecule. The sample (20-40 mesh) was first heated to 600 °C for 1 h in argon

atmosphere, then cooled to 120 °C. The Fourier Transform Infrared Spectrometer (FT-IR) spectra of all synthesized samples were measured using a PerkinElmer PE-100 Spectrum Frontier FT-IR spectrometer. Inductively coupled plasma (ICP) apparatus (Inductively Coupled Plasma, PerkinElmer 200) was applied for analysis of trace elements in the synthesized ZSM-22 samples. Prior to the characterization, 0.025 g of the ZSM-22 sample was mixed with 1.5 mL of 40 wt.% HF, which was added into a high-density polyethylene (HDPE) bottle. After that, 0.125mL of HNO_3 (45 wt.%), 0.375mL of HCl (45 wt.%) and 5 mL of distilled water are added to dissolve the ZSM-22 sample, followed by the addition of 12 mL saturated H_3BO_3 solution to avoid the Si evaporation. The solution is then diluted to 30 mL to be analyzed by ICP at last. The X-ray photoelectron spectroscopy (XPS) measurements were conducted on a Kratos, ULTRA AXIS DLD with an Al Ka achromatic X-ray source (1,486.6 eV) for all reduced catalysts. The NH_3 was injected and adsorbed for 30 min until saturated followed by the physical purging of argon. Finally, a programmed temperature increase (10 °C/min) to 650 °C was applied for NH_3 desorption, and a signal was recorded using a thermal conductivity detector (TCD). The Brønsted acidity of all samples was further characterized using a PerkinElmer PE-100 Spectrum Frontier FT-IR spectrometer. After vacuum pretreatment at 350 °C at 1.33×10^{-3} Pa for 2 h, the pyridine was introduced and adsorbed on the sample at 90 °C. After the adsorption is saturated, the temperature was raised to 200 and 350 °C respectively, and the desorption was carried out. According to the molar absorption coefficient[1,2], the total Brønsted acid density was calculated based on the band area at 1,540 cm^{-1} recorded at different temperatures. The calculation results by infrared spectra of adsorbed pyridine (Py-IR) recorded at 200 and 350 °C were the total and strong Brønsted acid density of the sample, respectively. The H_2 temperature-programmed reduction (H_2-TPR) of all samples and Pd dispersion of all catalysts were characterized by an Auto ChemII 2920 chemical adsorbent. For H_2-TPR, prior to measurements, the catalyst sample was treated with flowing Ar at 500 °C for 1 h. After the sample was cooled down to 50 °C, the gas was switched to 10% H_2/Ar. The sample was heated to 900 °C at a rate of 10 °C/min after the signal was stabilized. For the investigation of Pd dispersion, H_2 (40 mL/min) was used to reduce the metal oxide to metallic simple substance. The temperature was raised to 400 °C for 1 h. Then, Ar was introduced at 450 °C for 2 h, cooled to about 25 °C, and then the 10% H_2-Ar mixture was introduced in pulse form and adsorbed to saturation.

Catalytic tests for *n*-hexadecane hydroisomerization

All catalysts were tested for *n*-hexadecane hydroisomerization in a fixed-bed reactor. Before the reaction, 1 g of the calcined catalyst is placed in a constant temperature area of the tube and introduced into the hydrogen at 400 °C for 1 h reduction. The test conditions were 2.0 MPa pressure, 3.7 h^{-1} weight hourly space velocity (WHSV) and 500 H_2/*n*-hexadecane volume ratio. The product analysis was measured using a gas chromatograph (Agilent 7820) with a flame ionization detector (FID) and an HP-1 (60 m × 250 μm × 1 mm) capillary column.

The conversion of *n*-hexadecane, the selectivity of *iso*-hexadecane and the yield of *iso*-hexadecane were calculated using Equations (2-4):

$$\text{Conversion of } n\text{-hexadecane} = \frac{n-\text{hexadecane consumed}}{n-\text{hexadecane in feedstock}} \tag{2}$$

$$\text{Selectivity of } iso\text{-hexadecane} = \frac{iso-\text{hexadecane formed}}{n-\text{hexadecane consumed}} \tag{3}$$

$$\text{Yield of } iso\text{-hexadecane} = \frac{iso-\text{hexadecane formed}}{n-\text{hexadecane in feedstock}} \tag{4}$$

The n_{as} value, representative of the average acid steps of one *n*-hexadecane molecule contacted during the hydroisomerization between two Pd sites, was calculated according to the production distribution of
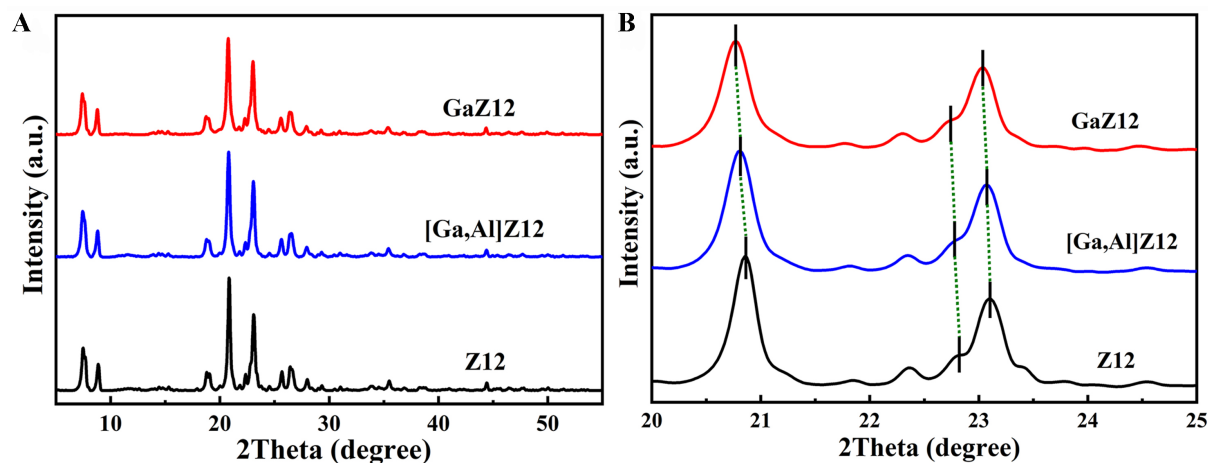
Figure 1. (A) XRD patterns of the Z12, [Ga,Al]Z12 and GaZ12 samples; and (B) locally enlarged 2θ patterns between 20° and 25° for the three samples. XRD: X-ray powder diffractometer.

n-hexadecane conversion of about 10% (within the dynamic control range) using Equation (5):

$$n_{as} = Mono \times 1 + Multi \times 2.5 + Cracked \times [4 + (N_C - 2) / 2] \tag{5}$$

in which the proportions of mono-branched *iso*-hexadecane, multi-branched *iso*-hexadecane and cracking products in the process of hydroisomerization are represented as "Mono", "Multi" and "Cracked", respectively. The N_C value represented the average number of molecules formed after the cleavage of each *n*-hexadecane molecule.

RESULTS AND DISCUSSION

Structure and morphology of the Z12, [Ga,Al]Z12 and GaZ12 samples

The XRD patterns of the Z12, [Ga,Al]Z12 and GaZ12 samples are shown in Figure 1. For all the samples, only the characteristic diffraction peaks ascribed to typical MTW structure are observed at approximately 7.6°, 8.8°, 20.9°, 22.9° and 23.3°, suggesting that the three samples are all pure [Figure 1A]. Moreover, the 2θ of the diffraction peaks for the three samples decreases as more Ga atoms are substituted in the samples [Figure 1B], which suggests that isomorphous substitution by Ga leads to a larger interplanar spacing. The crystal cell volume data listed in Table 1 show that the unit cell parameters and volume of the three samples both increase in the order of Z12 < [Ga,Al]Z12 < GaZ12, which originates from the longer Ga–O bond compared with the Al–O bonds for the GaZ12 and [Ga,Al]Z12 samples, with framework Al atoms being completely or partially isomorphously substituted by Ga atoms, respectively[33]. In addition to the unit cell size, the half-width of the diffraction peaks of the [Ga,Al]Z12 and GaZ12 samples also increases. Based on the Scherrer equation, the calculated average crystal size of the three samples demonstrates that Ga substitution effectively reduces the crystal size of synthesized ZSM-12 samples [Table 1].

Figure 2 shows SEM and TEM images of the Z12 [Figure 2A-C], [Ga,Al]Z12 [Figure 2D-F] and GaZ12 samples [Figure 2G-I]. The Z12 sample shows a morphology of spherical aggregates of about 1 μm, which are composed of nanocrystals of approximately 40-50 nm [Figure 2A and B]. For the partially and completely Ga isomorphous substituted [Ga,Al]Z12 and GaZ12 samples, the aggregates change to ellipsoidal shapes. Additionally, the sizes of the aggregates and single grains of [Ga,Al]Z12 decrease to 800-900 and 30-40 nm, respectively [Figure 2D and E]. For the GaZ12 sample, the aggregates and single grains

Table 1. The unit cell parameters and mean average sizes of the Z12, [Ga,Al]Z12 and GaZ12 samples based on the XRD patterns

Samples	Unit cell parameters (Å)			Unit cell volume (Å³)	Crystal size[a] (nm)
	A	b	c		
Z12	25.105	5.046	24.361	3,085.96	42
[Ga,Al]Z12	25.226	5.047	24.395	3,106.05	36
GaZ12	25.311	5.064	24.454	3,134.08	24

[a]Calculated according to Scherrer equation. XRD: X-ray powder diffractometer.
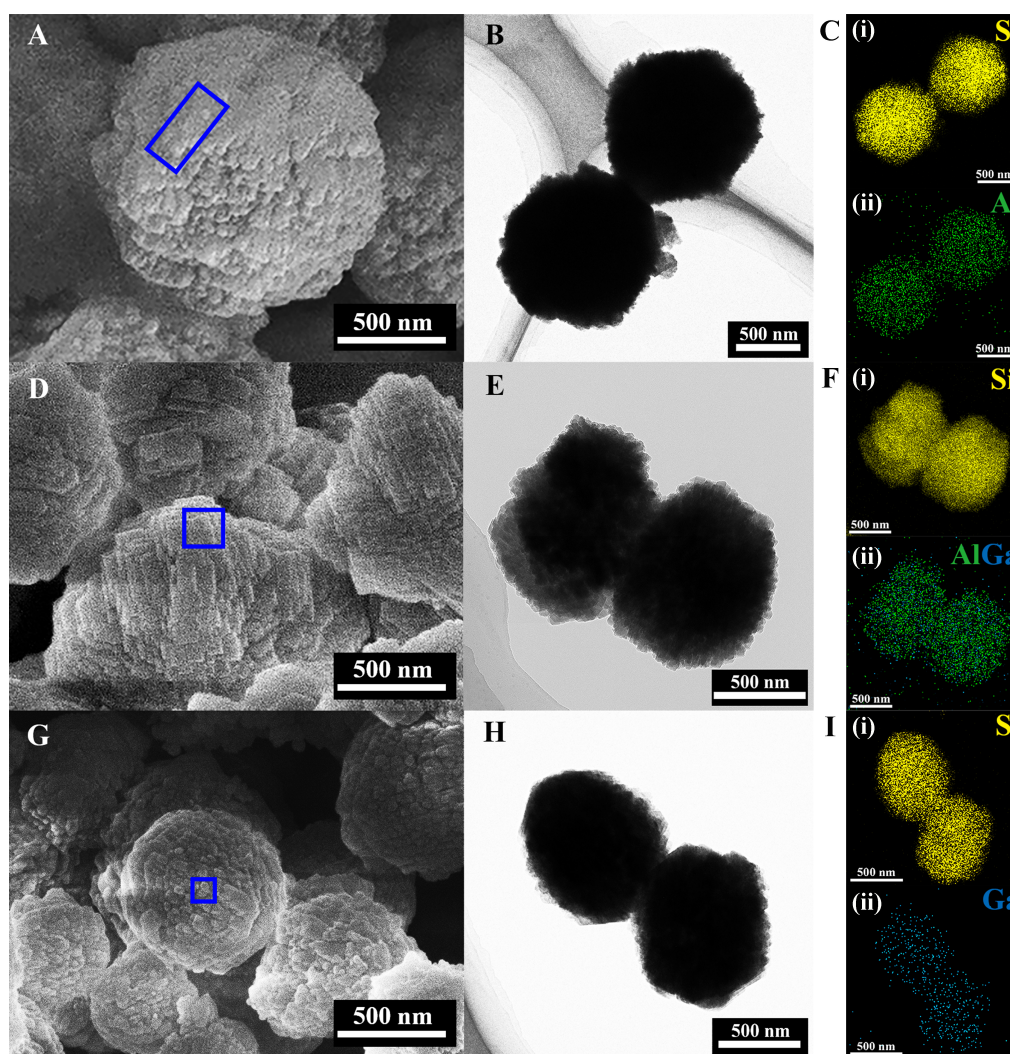

Figure 2. (A, D, G) SEM images, (B, E, H) TEM images, [C(i), F(i), I(i)] Si EDS mapping and [C(ii), F(ii), I(ii)] Al or/and Ga EDS mapping of the (A-C) Z12, (D-F) [Ga,Al]Z12 and (G-I) GaZ12 samples. SEM: Scanning electron microscopy; TEM: transmission electron microscopy; EDS: energy dispersive X-ray spectrometry.

further decrease to 600-700 and 20-30 nm, respectively [Figure 2G and H]. These phenomena are consistent with the calculated results based on the Scherrer equation, demonstrating that Ga isomorphous substitution is an effective method for reducing the size of synthesized ZSM-12 samples, which will be beneficial for improving the mass transfer properties of zeolite channels. Moreover, Si [Figure 2C(i), F(i) and I(i)], Al [Figure 2C(ii) and F(ii)] and Ga energy dispersive X-ray spectrometry (EDS) mappings [Figure 2F(ii) and

I(ii)] reveal that the corresponding Si, Al, and Ga atoms are dispersed well in the Z12, [Ga,Al]Z12 and GaZ12 samples, respectively.

For the N_2 adsorption-desorption isotherms of the Z12, [Ga,Al]Z12 and GaZ12 samples shown in Supplementary Figure 1, a steep adsorption curve at $P/P_0 < 0.01$, and the hysteresis loop observed at P/P_0 between 0.5-0.9 suggest the existence of micropores and intercrystal mesopores for all the samples. According to the isotherms, the surface area and pore volume of the samples were calculated and are shown in Table 2. Compared with those of Z12, the external surface area and mesopore volume of the [Ga,Al]Z12 and GaZ12 samples are both evidently larger, indicating a decrease in the crystal size and an increase in the mesoporosity.

The compositions of the Z12, [Ga,Al]Z12 and GaZ12 samples

^{27}Al, ^{71}Ga, and ^{29}Si MAS NMR were conducted to investigate the chemical environment of the synthesized Z12, [Ga,Al]Z12 and GaZ12 samples. As shown in Figure 3A and B, strong peaks at a chemical shift of 54 ppm are both found in the ^{27}Al MAS NMR spectra of the Z12 and [Ga,Al]Z12 samples, which corresponds to the tetracoordinated framework Al atoms. Furthermore, based on the ^{71}Ga MAS NMR spectra of the [Ga,Al]Z12 and GaZ12 samples in Figure 3C and D, the peaks ascribed to framework Ga atoms are observed at 150 ppm, and the peak intensity of the GaZ12 sample is much stronger than that of the [Ga,Al]Z12 sample. This phenomenon suggests that Ga atoms are successfully introduced into the ZSM-12 zeolite framework for the two samples and the amount of Ga atoms in the GaZ12 sample is much greater. Furthermore, the substitution of Ga atoms into the framework of the two synthesized samples was also confirmed by FT-IR spectroscopy [Supplementary Figure 2]. In the FT-IR spectra of the three samples, the absorption bands at approximately 1,220 and 1,100 cm^{-1} are ascribed to the asymmetric stretching vibration peaks of the Si–O band of the silica tetrahedron and the T–O–T bands of the MTW framework, respectively. In comparison with the Z12 sample, the wavenumbers of the T–O–T bands of the [Ga,Al]Z12 and GaZ12 samples shift toward lower wavenumbers with increasing Ga atoms substituted into the framework. This is because the Ga–O bond is longer than the Al–O bond, and the replacement of Ga instead of framework Al to form the Ga–O bond will cause a decrease in the force constant, which accordingly reduces the vibration frequency of the T–O–T bond of the [Ga,Al]Z12 and GaZ12 samples.

In the ^{29}Si MAS NMR spectra of the three samples [Supplementary Figure 3], four resonance peaks at chemical shifts of approximately -101, -105, -109 and -113 ppm are observed, which correspond to Si(3SiOH), Si(3Si1Al), and Si(4Si0Al) species in two different environments, respectively. The framework Si/(Al+Ga)$_{FW}$ ratios of the three samples were further calculated. Although the Si/(Al+Ga) ratios in the initial gel are the same [Table 3], the calculated Si/(Al+Ga)$_{FW}$ ratios of the three samples increase in the order of Z12 (63) < [Ga,Al]Z12 (70) < GaZ12 (89), suggesting that the substitution of Ga into the ZSM-12 framework is more difficult than that of Al.

In addition to the MAS NMR measurements, ICP and XPS characterizations were also conducted for the Z12, [Ga,Al]Z12 and GaZ12 samples to further determine the bulk Si/(Al+Ga)$_{Bulk}$ and the surface Si/(Al+Ga)$_{Surf}$ ratios. From Table 3 and Supplementary Table 1, the bulk Si/(Al+Ga)$_{Bulk}$ ratios of the three samples change in the same order as the framework Si/(Al+Ga)$_{FW}$ ratios. Moreover, the Si/(Al+Ga)$_{FW}$ ratios of each sample are slightly greater than the corresponding Si/(Al+Ga)$_{Bulk}$ ratios, demonstrating the existence of extraframework Al or Ga species in the synthesized samples. Moreover, the difference between the Si/(Al+Ga)$_{FW}$ and Si/(Al+Ga)$_{Bulk}$ ratios gradually increases for the [Ga,Al]Z12 and GaZ12 samples with Ga content, which can be attributed to the formation of more extraframework Al and/or Ga species because it is more difficult for Ga atoms to insert into the sample framework. Furthermore, the surface Si/(Al+Ga)$_{Surf}$

Table 2. The textural properties of the Z12, [Ga,Al]Z12 and GaZ12 samples

Samples	Surface area (m²/g)			Pore volume (cm³/g)		
	BET	Micropore[a]	External	Total[b]	Micropore[a]	Mesopore
Z12	342	300	42	0.226	0.118	0.108
[Ga,Al]Z12	337	275	62	0.265	0.109	0.156
GaZ12	334	258	76	0.255	0.103	0.152

[a]Determined by t-plot method; [b]Volume adsorbed at $P/P_0 = 0.99$. BET: Brunauer-Emmett-Teller method.

Table 3. Chemical components of the Z12, [Ga,Al]Z12 and GaZ12 samples

Samples	Chemical compositions			
	Si/(Al+Ga)$_{Gel}$	Si/(Al+Ga)$_{Bulk}$[a]	Si/(Al+Ga)$_{FW}$[b]	Si/(Al+Ga)$_{Surf}$[c]
Z12	65	62	63	27
[Ga,Al]Z12	65	67	70	17
GaZ12	65	86	89	43

[a]By the ICP method; [b]by ^{29}Si MAS NMR spectroscopy; [c]Calculated from XPS data. ICP: Inductively coupled plasma; MAS: magic angle spinning; NMR: nuclear magnetic resonance; XPS: X-ray photoelectron spectroscopy.
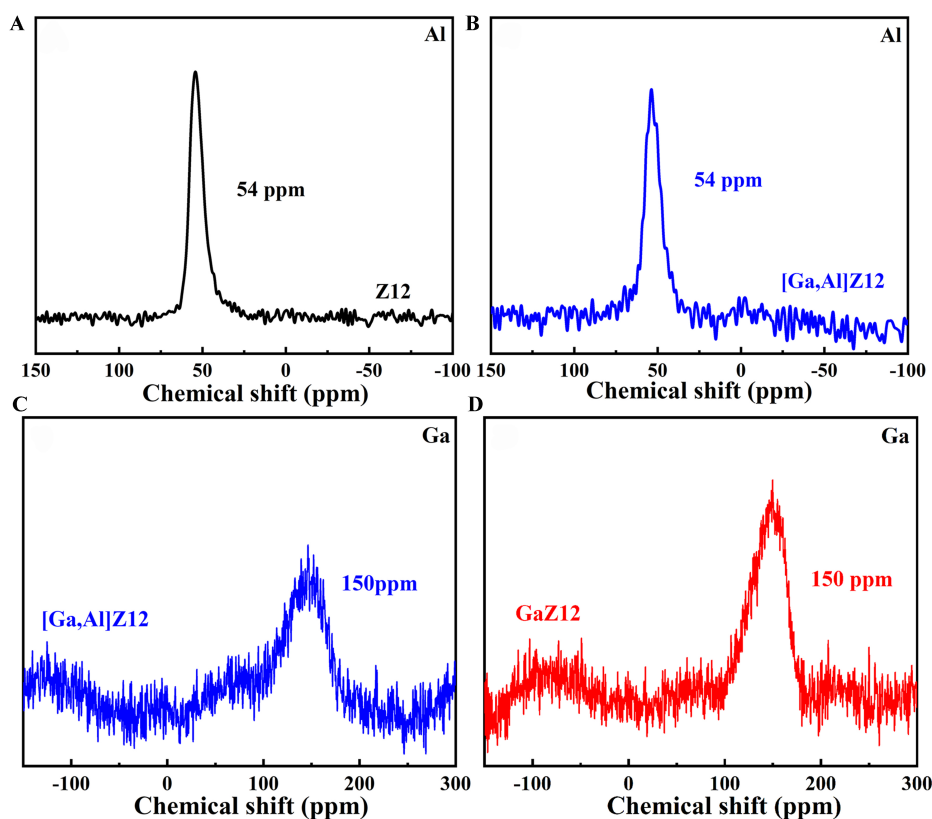

Figure 3. ^{27}Al MAS NMR spectra of the (A) Z12 and (B) [Ga,Al]Z12 samples and ^{71}Ga MAS NMR spectra of the (C) [Ga,Al]Z12 and (D) GaZ12 samples. MAS: Magic angle spinning; NMR: nuclear magnetic resonance.

ratios determined by the XPS method for each sample are significantly lower than the corresponding Si/(Al+Ga)$_{FW}$ and Si/(Al+Ga)$_{Bulk}$ ratios, indicating that more Al or Ga atoms are dispersed on the external surface rather than existing inside the ZSM-12 crystal. Furthermore, the total amount of framework Al and

Ga atoms in the [Ga,Al]Z12 sample is the lowest among the three samples since Ga and Al atoms compete to be inserted into the sample framework during crystallization, which leads to an increase in the amount of both non-framework Al and Ga species and, thus, the lowest $Si/(Al+Ga)_{Surf}$ ratios.

Furthermore, from the XPS spectra of the [Ga,Al]Z12 and GaZ12 samples [Figure 4], the peak at a binding energy of 1,118.5 eV is attributed to the Ga_2O_3 species located at the external surface, while the peak at 1,119.4 eV is ascribed to the Ga species located in the micropores or that interact strongly with the negatively charged framework of the synthesized samples[34]. The existence of the two kinds of Ga species at different locations was also proven by H_2-TPR measurements. From Supplementary Figure 4, two reduction peaks exist between 230 and 440 °C for the [Ga,Al]Z12 and GaZ12 samples, which are not found for the Z12 sample. The reduction peak at lower temperatures originates from the reduction of Ga_2O_3 species on the surface of synthesized crystals, and the peak observed at higher temperatures corresponds to the reduction of Ga species located in the channel or that interact strongly with the negatively charged sample framework.

Acidity of the Z12, [Ga,Al]Z12 and GaZ12 samples

The acidity of the Z12, [Ga,Al]Z12 and GaZ12 samples was characterized by NH_3-TPD. For the three samples, two NH_3 desorption peaks at varying temperatures are found in the NH_3-TPD curves, which originate from the desorption of NH_3 from weak and strong acid sites of the samples, respectively [Supplementary Figure 5]. Compared with those of the weak acid sites, the temperature of the desorption peak of NH_3 from the strong acid sites evidently decreases as the amount of framework Ga atoms increases for the three samples, indicating a much weaker acid strength of the strong acid sites for the Ga isomorphous substituted samples [Table 4]. This result originates from the electronegativity difference between Ga and Al atoms. For the [Ga,Al]Z12 and GaZ12 samples, Ga atoms are substituted in the framework to form Ga-OH-Si groups. Since the electronegativity of the Ga atoms is greater than that of the Al atoms in the Al-OH-Si groups, the bond energy of Ga–O bonds is lower. As a result, H^+ is more difficult to dissociate from Ga-OH-Si groups, and the Brønsted acid sites of the [Ga,Al]Z12 and GaZ12 samples are accordingly weaker, which causes the weaker strength of the strong acid sites compared with that of the Z12 sample.

Since Brønsted acid sites are responsible for isomerization and cracking, quantitatively determining the Brønsted acid density from the Py-IR is more important. As shown in Supplementary Figure 6, two characteristic adsorption peaks appear at ~1,455 and ~1,545 cm^{-1} in the Py-IR of Z12, [Ga,Al]Z12 and GaZ12 samples, which are attributed to Lewis and Brønsted acid sites, respectively. Compared with those of the Z12 sample, the total and strong Brønsted acid densities of the [Ga,Al]Z12 and GaZ12 samples both decrease as the Ga amount in the samples increases because of the decreasing total amount of framework Ga and Al atoms [Table 4]. As a result, fewer frameworks bridging hydroxyl groups $Si-O(H^+)$-Ga and $Si-O(H^+)$-Al to provide Brønsted acid sites are formed, so that the Brønsted acid density of the [Ga,Al]Z12 and GaZ12 samples both decrease, and the GaZ12 sample demonstrates the lowest Brønsted acid density. Additionally, the Lewis acid density of the three samples changes in the opposite order as the Brønsted acid density, which originates from the more extra-framework Al or/and Ga species.

Characteristics of the prepared bifunctional catalysts

According to previous reports, bifunctional catalysts with appropriate metal-acid proximity by locating metal sites on the Al_2O_3 instead of zeolite generally demonstrate improved catalytic performance for the *n*-alkane hydroisomerization[35,36]. Therefore, 0.6 wt.% Pd was first loaded on γ-Al_2O_3 (0.6Pd/A sample) and then mixed with the Z12, [Ga,Al]Z12 and GaZ12 zeolite samples, respectively, by a mass ratio of 1:1 to prepare corresponding 0.3Pd/A-Z12, 0.3Pd/A-[Ga,Al]Z12 and 0.3Pd/A-GaZ12 catalysts with moderate metal-acid proximity. For comparison, a bifunctional catalyst with the closest metal-acid proximity by

Table 4. The desorption temperatures of NH$_3$ and acid density of the Z12, [Ga,Al]Z12 and GaZ12 samples

Samples	T$_{wd}$[a] (°C)	T$_{sd}$[b] (°C)	Brønsted acid density (μmol·g^{-1})		Lewis acid density (μmol·g^{-1})
			Strong	Total	Total
Z12	168	362	26.7	31.2	10.2
[Ga,Al]Z12	168	338	24.4	29.3	15.8
GaZ12	168	313	20.3	25.3	23.8

[a]T$_{wd}$ represents the lower desorption temperature of NH$_3$; [b]T$_{sd}$ represents the higher desorption temperature of NH$_3$.
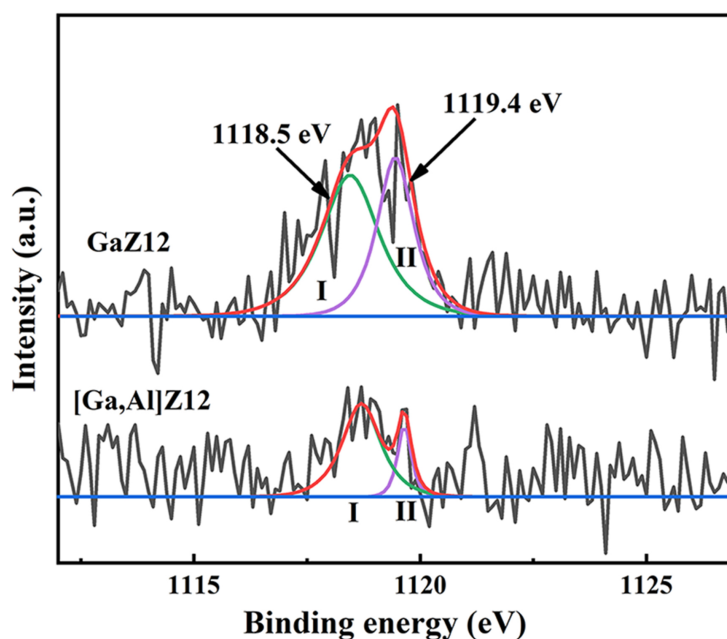

Figure 4. The Ga 2p XPS spectra of the [Ga,Al]Z12 and GaZ12 samples. XPS: X-ray photoelectron spectroscopy.

mixing 0.6Pd/Z12 (by loading 0.6 wt.% Pd on ZSM-12 zeolite) and γ-Al$_2$O$_3$ with a mass ratio of 1:1 was also prepared and named 0.3Pd/Z12-A. The XRD patterns of four bifunctional catalysts are shown in Supplementary Figure 7. The XRD patterns of the four catalysts fit well with those of the corresponding unsupported zeolites except the broad band of Al$_2$O$_3$ around 2θ values of 46°. Simultaneously, no peaks attributed to Pd were observed. This result suggests that the deposited Pd nanoparticles with low loading are highly dispersed on Al$_2$O$_3$ or zeolites[37]. From Supplementary Table 2, the microporous surface area and volume of the four catalysts are evidently lower compared with the corresponding zeolite sample. Additionally, the 0.3Pd/Z12-A catalyst shows the lowest total and strong Brønsted acid density, which can be attributed to partial blocking of the micropores by the deposited Pd nanoclusters [Table 5]. In addition, the 0.3Pd/Z12-A catalyst also reveals the lowest Pd dispersion of 27.2%, and the other three catalysts with a Pd loading on γ-Al$_2$O$_3$ demonstrated the same Pd dispersion of 39.4% and a Pd site amount of 11.11 μmol·g^{-1} since they were prepared with the same 0.6Pd/A sample. As a result, the C$_{Pd}$/C$_{H+}$ ratio of exposed Pd atoms (C$_{Pd}$ value) to the total Brønsted acid density (both listed in Table 5) for the four catalysts increased in the following order: 0.3Pd/A-Z12 < 0.3Pd/Z12-A < 0.3Pd/A-[Ga,Al]Z12 < 0.3Pd/A-GaZ12. It has been proven that a higher C$_{Pd}$/C$_{H+}$ ratio is generally beneficial for suppressing the cracking of intermediates owing to the stronger metal functionality and rapid hydrogenation to form *iso*-alkane products accordingly[38,39]. Therefore, isomorphously substituting ZSM-12 zeolite with Ga can appropriately reduce the Brønsted acid density, improve the Pd dispersion and adjust the metal-acid balance.

Table 5. Characteristics of 0.3Pd/A-Z12, 0.3Pd/A-[Ga,Al]Z12 and 0.3Pd/A-GaZ12 bifunctional catalysts

| Samples | Brønsted acid density (μmol·g⁻¹) | | D_{Pd} (%)[a] | C_{Pd} (μmol·g⁻¹)[b] | C_{Pd}/C_{H+}[c] |
	Strong	Total			
0.3Pd/Z12-A	8.9	10.5	27.2	7.7	0.733
0.3Pd/A-Z12	13.4	15.6	39.4	11.1	0.712
0.3Pd/A-[Ga,Al]Z12	12.2	14.7	39.4	11.1	0.756
0.3Pd/A-GaZ12	10.2	12.7	39.4	11.1	0.875

[a]Determined by H_2 chemisorption; [b]Calculated by D_{Pd}; [c]Calculated by total Brønsted acid density.

_n_-hexadecane hydroisomerization over bifunctional catalysts

Figure 5A and B shows that, for the 0.3Pd/Z12-A, 0.3Pd/A-Z12, 0.3Pd/A-[Ga,Al]Z12 and 0.3Pd/A-GaZ12 catalysts, the *n*-hexadecane conversion all demonstrate typical S-shaped curves as reaction temperature increases. Compared with the 0.3Pd/Z12-A catalyst with Pd deposited directly on ZSM-12 zeolite and the closest metal-acid proximity (metal-acid distance on atomic scale), the 0.3Pd/A-Z12 catalyst with Pd loaded on the γ-Al_2O_3 exhibited improved catalytic activity due to the higher Brønsted acid density [Table 5]. For the 0.3Pd/A-Z12, 0.3Pd/A-[Ga,Al]Z12 and 0.3Pd/A-GaZ12 catalysts (metal-acid distance on micrometer scale) with the same metal-acid proximity, the *n*-hexadecane conversion decreased at the same temperature as the Ga amount increased because of their weaker Brønsted acidity after isomorphous substitution by Ga [Figure 5B].

The *iso*-hexadecane yields over the four catalysts are shown in Figure 5C and D. The 0.3Pd/Z12-A catalyst demonstrates a maximum *iso*-hexadecane yield of 69.9%, while for the 0.3Pd/A-Z12 catalyst, the maximum *iso*-hexadecane yield increases to 74.3%. This result indicates that appropriate metal-acid proximity for the 0.3Pd/A-Z12 catalyst is evidently beneficial for the promotion of the *iso*-hexadecane yield. For the 0.3Pd/Z12-A catalyst, the intermediates generated on Pd sites loaded on ZSM-12 zeolite then diffuse to the Brønsted acid sites on the ZSM-12 zeolite so that further isomerization and even cracking easily occur due to their limited diffusion in the micropore channel. However, for the 0.3Pd/A-Z12 catalyst, the intermediates are generated on Pd sites loaded on γ-Al_2O_3 and then diffuse to the Brønsted acid sites on the surface or at the opening of ZSM-12 zeolite instead of diffusing into the micropores, which can effectively limit the cracking of these intermediates due to the avoidance of diffusion into micropores[36]. As a result, the maximum *iso*-hexadecane yield over the 0.3Pd/A-Z12 catalyst was higher. Furthermore, the maximum *iso*-hexadecane yield over the 0.3Pd/A-[Ga,Al]Z12 catalyst increased to 77.9% [Figure 5D]. The 0.3Pd/A-GaZ12 catalyst demonstrated the maximum *iso*-hexadecane yield of 80.6%, which is much greater than that reported in previous works [Supplementary Table 3] and is 6.3% higher compared with the 0.3Pd/A-Z12 catalyst. Moreover, the n_{as} values (the acid steps that the alkene intermediates undergo between two Pd sites) were calculated. The n_{as} for the four catalysts decreased as 0.3Pd/Z12-A (1.81) > 0.3Pd/A-Z12 (1.62) > 0.3Pd/A-[Ga,Al]Z12 (1.49) > 0.3Pd/A-GaZ12 (1.38) [Supplementary Table 4]. Owing to the avoidance of diffusion of the intermediates into micropores, the n_{as} value of 0.3Pd/A-Z12 is only 1.62, which leads to a higher maximum *iso*-hexadecane yield compared with the 0.3Pd/Z12-A catalyst. For the 0.3Pd/A-[Ga,Al]Z12 and 0.3Pd/A-GaZ12 catalysts, the increase in the number of substituted Ga atoms further reduces the Brønsted acid strength and density and effectively increases their C_{Pd}/C_{H+} ratios, which makes the metal-acid balance of the bifunctional catalysts more favorable and reveal lower n_{as} during hydroisomerization. In addition, the crystal sizes of Ga-substituted ZSM-12 samples are also reduced, which causes greater mesoporosity and improved diffusion of alkene intermediates, resulting in effectively limiting the cracking of intermediates over the 0.3Pd/A-[Ga,Al]Z12 and 0.3Pd/A-GaZ12 catalysts, so that the maximum *iso*-hexadecane yield is promoted.
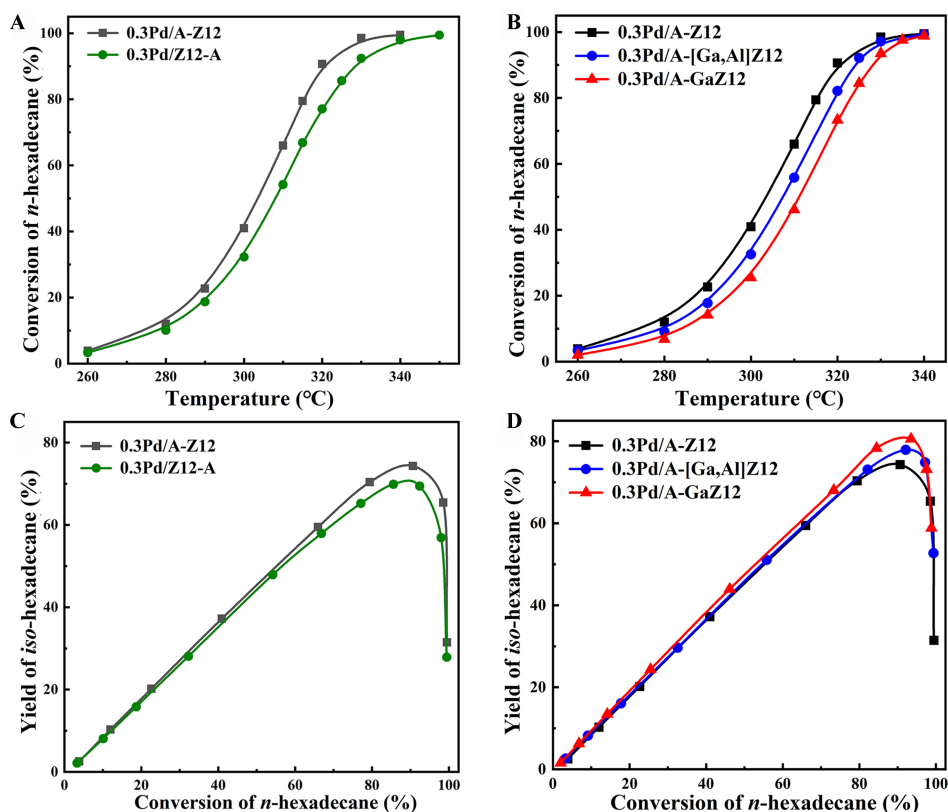
Figure 5. (A and B) The *n*-hexadecane conversion; and (C and D) the *iso*-hexadecane yield over different catalysts. The test conditions were 2.0 MPa pressure, 3.7 h^{-1} space velocity (WHSV) and 500 H$_2$/*n*-hexadecane volume ratio. WHSV: Weight hourly space velocity.

To further study the effects of Ga isomorphous substitution on the *n*-hexadecane hydroisomerization, the product distribution and the proportion of cracking products at the maximum yield of *iso*-hexadecane [Figure 6], as well as the product distribution in the kinetic control region [Supplementary Figure 8] over the catalysts, were investigated. From Supplementary Figure 8, when the conversion *n*-hexadecane is 9%~14%, the mono-branched *iso*-hexadecanes are the main products for the three catalysts. Meanwhile, when the conversion is higher (90%~93%), the main products are the multi-branched *iso*-hexadecanes for the three catalysts [Figure 6A]. As the Ga amount in the isomorphously substituted ZSM-12 zeolite rises, the quantity of multi-branched *iso*-hexadecanes also grows, while the distribution of cracking products decreases. In particular, for the 0.3Pd/A-GaZ12 catalyst, the multi-branched *iso*-hexadecanes distribution (64.6%) was the highest among the three catalysts. This result originates from the smaller grains and more openings of the 0.3Pd/A-GaZ12 catalyst, which can promote further isomerization to form multi-branched *iso*-hexadecanes. Simultaneously, its weaker acid strength also inhibits the further cracking of the multi-branched products. Therefore, the largest distribution of multi-branched *iso*-hexadecanes has been obtained for the 0.3Pd/A-GaZ12 catalyst. Furthermore, from the cracking product distribution shown in Figure 6B, the proportion of C$_3$-C$_6$ cracked products over the 0.3Pd/A-GaZ12 catalyst is evidently reduced, and the proportion of C$_8$-C1$_2$ liquid hydrocarbons is greater. This phenomenon demonstrates that Ga isomorphous substitution can also suppress the secondary cracking owing to the reduced acid strength and increase in the C$_{Pd}$/C$_{H+}$ ratio.

CONCLUSIONS

Herein, the effective method for *in situ* synthesis of [Ga,Al]Z12 and GaZ12 samples is established, in which
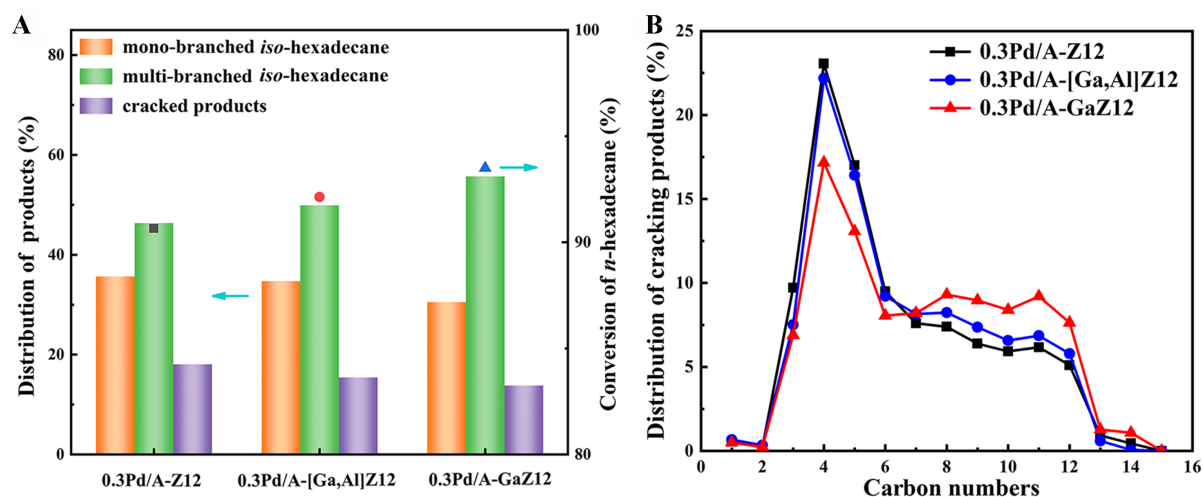
Figure 6. (A) Products distribution and (B) the proportion of cracking products at the maximum *iso*-hexadecane yield over 0.3Pd/A-Z12, 0.3Pd/A-[Ga,Al]Z12 and 0.3Pd/A-GaZ12 bifunctional catalysts. The test conditions were 2.0 MPa pressure, 3.7 h^{-1} space velocity (WHSV) and 500 H$_2$/*n*-hexadecane volume ratio. WHSV: Weight hourly space velocity.

framework Al atoms are partially or completely isomorphously substituted by Ga atoms. The characteristic results indicate that the Ga-substituted [Ga,Al]Z12 and GaZ12 samples have a greater mesoporosity and weaker Brønsted acidity compared with the Z12 silica aluminate sample. The 0.3Pd/A-Z12, 0.3Pd/A-[Ga,Al]Z12 and 0.3Pd/A-GaZ12 catalysts with appropriate metal-acid proximity are prepared by mixing 0.6Pd/A sample with 0.6 wt.% Pd loading on γ-Al$_2$O$_3$ and the corresponding ZSM-12 samples. These catalysts show higher *iso*-hexadecane yield for the *n*-hexadecane hydroisomerization in comparison with the 0.3Pd/Z12-A catalyst with 0.6 wt.% Pd directly deposited on ZSM-12 zeolite with closer metal-acid proximity. The enhanced mesoporosity, milder acidity and larger C$_{Pd}$/C$_{H+}$ ratio of the 0.3Pd/A-[Ga,Al]Z12 and 0.3Pd/A-GaZ12 bifunctional catalysts are beneficial for improving the *iso*-hexadecane yield and distribution of multi-branched *iso*-hexadecane products due to the achievement of more favorable metal-acid balance and effectively suppressed cracking of *iso*-olefin intermediates. The 0.3Pd/A-GaZ12 catalyst reveals a maximum *iso*-hexadecane yield of 80.6% and a proportion of multi-branched *iso*-hexadecane of 64.6%. Therefore, this work demonstrates an applicable method for the preparation of effective bifunctional catalysts to produce second-generation biodiesel with *iso*-alkanes as the main components via the hydroisomerization of long-chain *n*-alkanes.

DECLARATIONS

Authors' contributions
Writing-original draft, methodology, visualization, investigation, formal analysis, data curation: Lin H
Investigation: Xu C
Writing-original draft, visualization, software, data curation, validation, funding acquisition: Wang W
Conceptualization, methodology, resources, writing-reviewing and editing, funding acquisition, supervision, project administration: Wu W

Availability of data and materials
Since parts of the data of the article involves the cooperation with other companies, we cannot make all data applicable. However, if some researchers are interested in our work and want to reproduce it, they can contact us directly and we will provide the corresonding data.

Financial support and sponsorship

Conflicts of interest

All authors declared that there are no conflicts of interest.

Ethical approval and consent to participate

Not applicable.

Consent for publication

Not applicable.

Copyright

REFERENCES

1.   Fan L, Lyu Y, Fu J, et al. Metal particle size effects over the Ni/SAPO-11 bifunctional catalyst. *Appl Surf Sci* 2023;636:157736. DOI

2.   Ding S, Parlett CM, Fan X. Recent developments in multifunctional catalysts for fatty acid hydrodeoxygenation as a route towards biofuels. *Mol Catal* 2022;523:111492. DOI

3.   Chen LH, Sun MH, Wang Z, Yang W, Xie Z, Su BL. Hierarchically structured zeolites: from design to application. *Chem Rev* 2020;120:11194-294. DOI PubMed

4.   Wu Q, Luan H, Xiao F. Theoretical design for zeolite synthesis. *Sci China Chem* 2022;65:1683-90. DOI

5.   Yuan K, Jia X, Wang S, et al. Effect of crystal size of ZSM-11 zeolite on the catalytic performance and reaction route in methanol to olefins. *Chem Synth* 2023;4:31. DOI

6.   Niu P, Liu P, Xi H, et al. Design and synthesis of Pt/ZSM-22 catalysts for selective formation of iso-Dodecane with branched chain at more central positions from *n*-Dodecane hydroisomerization. *Appl Catal A Gen* 2018;562:310-20. DOI

7.   Yang C, Wang W, Wang D, et al. The promotion effects of MoOx species in the highly effective NiMo/MgAl$_2$O$_4$ catalysts for the hydrodeoxygenation of methyl palmitate. *J Environ Chem Eng* 2022;10:107761. DOI

8.   Lyu Y, Yu Z, Yang Y, et al. Metal and acid sites instantaneously prepared over Ni/SAPO-11 bifunctional catalyst. *J Catal* 2019;374:208-16. DOI

9.   Tan Y, Zhao Y, Li H, et al. Inhibition of terminal C–C bonds cleavage drives high selectivity of *n*-alkane hydroisomerization. *J Catal* 2023;428:115144. DOI

10. Xiong S, Sun J, Li H, Wang W, Wu W. The synthesis of hierarchical ZSM-22 zeolite with only the PHMB template for hydroisomerization of *n*-hexadecane. *Micropor Mesopor Mat* 2024;365:112895. DOI

11. Wang W, Liu C, Wu W. Bifunctional catalysts for the hydroisomerization of *n*-alkanes: the effects of metal-acid balance and textural structure. *Catal Sci Technol* 2019;9:4162-87. DOI

12. He L, Fu W, Li L, et al. Study of CA-treated ZSM-22 zeolite with enhanced catalytic performance in the hydroisomerization of long-chain *n*-dodecane. *New J Chem* 2021;45:2820-9. DOI

13. Han Y, Yuan J, Xing M, et al. Shape selectivity of zeolite for hydroisomerization of long-chain alkanes. *New J Chem* 2023;47:1401-12. DOI

14. Li S, Mezari B, Wu H, Kosinov N, Hensen EJ. ZSM-12 nanocrystals with tunable acidity directed by rigid diquats: synthesis and catalytic applications. *Fuel* 2023;333:126363. DOI

15. Wang S, Wang C, Liu H, et al. Acceleration effect of sodium halide on zeolite crystallization: ZSM-12 as a case study. *Micropor Mesopor Mat* 2022;331:111652. DOI

16. Lu X, Guo Y, Zhang Y, Ma R, Fu Y, Zhu W. Enhanced catalytic activity of Pt/H-ZSM-12 via alkaline post-treatment for the hydroisomerization of n-hexane. *Micropor Mesopor Mat* 2020;306:110459. DOI

17. Liu J, Yang H, Song Z, Sun J, Guo X. Isomerization of *n*-dodecane for high selectivity of multibranched iso-dodecane over Pt/ZSM-22 - Y catalyst. *Ind Eng Chem Res* 2023;62:21112-9. DOI

18. Guo K, Ma A, Wang Z, et al. Investigation of *n*-heptane hydroisomerization over alkali-acid-treated hierarchical Pt/ZSM-22 zeolites. *New J Chem* 2022;46:16752-63. DOI

19. Zhang L, Liu N, Dai C, et al. Recent advances in shape selectivity of MFI zeolite and its effect on the catalytic performance. *Chem Synth* 2023;3:2. DOI

20. Sun J, Xiong S, Wu Q, Wang W, Wu W. The preparation of nanosized Pd/ZSM-23 bifunctional catalysts for *n*-hexadecane hydroisomerization by employing PHMB as the growth modifier. *Trans Tianjin Univ* 2023;29:482-91. DOI

21. Li X, Sun M, Rooke JC, Chen L, Su B. Synthesis and applications of hierarchically porous catalysts. *Chinese J Catal* 2013;34:22-47. DOI

22. Sun J, Xiong S, Lin H, et al. The effects of growth modifiers on the catalytic performance of hierarchical Pd/ZSM-23 bifunctional

catalysts for n-hexadecane hydroisomerization. *Fuel* 2023;347:128406. DOI

23. Lari GM, Mondelli C, Pérez-ramírez J. Gas-phase oxidation of glycerol to dihydroxyacetone over tailored iron zeolites. *ACS Catal* 2015;5:1453-61. DOI

24. Yabushita M, Kobayashi H, Osuga R, et al. Mechanochemical approach to preparation of MFI zeolites substituted isomorphously by both Al and Fe as durable catalysts for the dimethyl ether to olefin reaction. *Ind Eng Chem Res* 2021;60:2079-88. DOI

25. Liu S, Ren J, Zhu S, et al. Synthesis and characterization of the Fe-substituted ZSM-22 zeolite catalyst with high *n*-dodecane isomerization performance. *J Catal* 2015;330:485-96. DOI

26. Geerts L, Ramachandran RK, Dendooven J, et al. Creation of gallium acid and platinum metal sites in bifunctional zeolite hydroisomerization and hydrocracking catalysts by atomic layer deposition. *Catal Sci Technol* 2020;10:1778-88. DOI

27. Al-yassir N, Akhtar MN, Al-khattaf S. Physicochemical properties and catalytic performance of galloaluminosilicate in aromatization of lower alkanes: a comparative study with Ga/HZSM-5. *J Porous Mater* 2012;19:943-60. DOI

28. Su X, Wang G, Bai X, et al. Synthesis of nanosized HZSM-5 zeolites isomorphously substituted by gallium and their catalytic performance in the aromatization. *Chem Eng J* 2016;293:365-75. DOI

29. Shang S, Li W, Zhou A, et al. Fe-substituted Pt/HZSM-48 for superior selectivity of *i*-C$_{12}$ in *n*-dodecane hydroisomerization. *Ind Eng Chem Res* 2022;61:1056-65. DOI

30. Dai X, Li L, Cheng Y, et al. In-situ synthesis of gallium-containing SAPO-11 molecular sieves and superior catalytic performance of their NiWS supported catalysts for hydroisomerization of *n*-hexadecane. *Eur J Inorg Chem* 2023;26:e202200557. DOI

31. Yang Z, Cao J, Zhu C, et al. In situ reforming of lignite pyrolysis volatiles for enriching light aromatics over Ga substituted HZSM-5. *Chem Eng Sci* 2022;248:117235. DOI

32. Liu S, He Y, Zhang H, et al. Design and synthesis of Ga-doped ZSM-22 zeolites as highly selective and stable catalysts for *n*-dodecane isomerization. *Catal Sci Technol* 2019;9:2812-27. DOI

33. Vieira LH, Carvalho KT, Urquieta-gonzález EA, Pulcinelli SH, Santilli CV, Martins L. Effects of crystal size, acidity, and synthesis procedure on the catalytic performance of gallium and aluminum MFI zeolites in glycerol dehydration. *J Mol Catal A Chem* 2016;422:148-57. DOI

34. Su X, Fang Y, Gao P, et al. In-situ microwave synthesis of nano-GaZSM-5 bifunctional catalysts with controllable location of active GaO^{+} species for olefins aromatization. *Micropor Mesopor Mat* 2020;306:110388. DOI

35. Zečević J, Vanbutsele G, de Jong KP, Martens JA. Nanoscale intimacy in bifunctional catalysts for selective conversion of hydrocarbons. *Nature* 2015;528:245-8. DOI PubMed PMC

36. Guo C, Wang W, Zhang Y, et al. Influences of the metal-acid proximity of Pd-SAPO-31 bifunctional catalysts for n-hexadecane hydroisomerization. *Fuel Process Technol* 2021;214:106717. DOI

37. Wang D, Liu J, Cheng X, et al. Trace Pt clusters dispersed on SAPO-11 promoting the synergy of metal sites with acid sites for high-effective hydroisomerization of *n*-alkanes. *Small Methods* 2019;3:1800510. DOI

38. Thybaut JW, Marin GB. Chapter two - Multiscale aspects in hydrocracking: from reaction mechanism over catalysts to kinetics and industrial application. *Adv Catal* 2016;59:109-238. DOI

39. Alvarez F, Ribeiro F, Perot G, Thomazeau C, Guisnet M. Hydroisomerization and hydrocracking of alkanes: 7. Influence of the balance between acid and hydrogenating functions on the transformation of *n*-decane on PtHY catalysts. *J Catal* 1996;162:179-89. DOI